Supporting Information

Dual-atomic Cu–Ag pairs boosting selective electroreduction of CO_2 to acetate

Zemin Feng, Chenghong Hu, Huangcong Tang, Kui Shen, Liyu Chen*, Yingwei Li*

Guangdong Provincial Key Laboratory of Fuel Cell Technology, School of Chemistry and Chemical Engineering, South China University of Technology, Guangzhou 510640, China.

E-mail: liyuchen@scut.edu.cn; liyw@scut.edu.cn

Experimental Section

Materials

Zinc nitrate hexahydrate ($Zn(NO_3)_2 \cdot 6H_2O$, 98%) was obtained from Guangzhou Chemical Reagent Factory. Copper nitrate trihydrate ($Cu(NO_3)_2 \cdot 3H_2O$, 99%), silver nitrate ($AgNO_3$, 99%), 2-methylimidazole ($C_4H_6N_2$, 98%), and potassium bicarbonate ($KHCO_3$, 99%) were purchased from Shanghai Aladdin Co., Ltd. Methanol (CH_3OH, 99%), isopropanol (C_3H_8O, 99%), and ethanol (CH_3CH_2OH, 99%) were provided by Guangdong Guanghua Sci-Tech Co., Ltd. All chemicals were used as received without further purification.

Preparation of ZIF-8(Cu/Ag), ZIF-8(Cu), ZIF-8(Ag), and ZIF-8

Synthesis of ZIF-8(Cu/Ag). Firstly, 0.89 g of $Zn(NO_3)_2 \cdot 6H_2O$, 0.086 g of $Cu(NO_3)_2 \cdot 3H_2O$, and 0.106 g $AgNO_3$ were dissolved in 30 mL of CH_3OH and 30 mL of H_2O under continuous stirring for ten minutes (labeled as solution A). Separately, 3 g of 2-methylimidazole was dissolved in 30 mL of methanol (labeled as solution B). Solution A was then added dropwise to solution B using a constant pressure funnel and allowed to react at room temperature for 2 h. The product was then centrifuged, washed with methanol and deionized water, and dried in a vacuum oven at 60 °C for 12 h, yielding ZIF-8(Cu/Ag). ZIF-8(Cu/Ag 1:1) and ZIF-8(Cu/Ag 5:1) were synthesized by adjusting the content of Cu and Ag.

Synthesis of ZIF-8(Cu). ZIF-8(Cu) was synthesized by following the same procedure as ZIF-8(Cu/Ag), excluding the addition of $AgNO_3$.

Synthesis of ZIF-8(Ag). ZIF-8(Ag) was synthesized by following the same procedure as ZIF-8(Cu/Ag), excluding the addition of $Cu(NO_3)_2 \cdot 3H_2O$.

Synthesis of ZIF-8. ZIF-8 was synthesized by following the same procedure as ZIF-8(Cu/Ag), excluding the addition of $AgNO_3$ and $Cu(NO_3)_2 \cdot 3H_2O$.

Synthesis of Cu–Ag/NC, Cu/NC, Ag/NC, and NC catalysts

Cu–Ag/NC electrocatalysts were synthesized by pyrolysis. ZIF-8(Cu/Ag) was placed in a small quartz porcelain boat and pyrolyzed for 2 h at 950 °C in a tube furnace under flowing Ar atmosphere to obtain Cu–Ag/NC.

Cu/NC, Ag/NC, NC, Cu–Ag/NC(1:1), and Cu–Ag/NC(5:1) were synthesized by following the same procedure as Cu–Ag/NC with ZIF-8(Cu), ZIF-8(Ag), ZIF-8, ZIF-8(Cu/Ag 1:1), and ZIF-8(Cu/Ag 5:1) as precursors, respectively.

Catalyst characterizations

Powder X-ray diffraction (XRD) patterns were recorded using a Rigaku diffractometer (D8 ADVANCE) with Cu Kα radiation (60 kV, 30 mA, $\lambda = 0.1543$ nm). N_2 sorption measurements were conducted at 77 K using a Tristar ll 3020 instrument. The morphology of the materials was investigated by high-resolution scanning electron microscopy (Regulus 8100). The structure and element mapping were determined by a high-resolution transmission electron microscope (TEM, JEOL, JEM-2100F) with EDS analysis (Bruker Xflash 5030 T) operated at 200 kV. The atomic structure of Cu–Ag/NC was characterized using transmission electron microscopy (Thermo Scientific Themis Z) equipped with double spherical aberration correctors. The metal contents of the samples were determined by inductively coupled plasma optical emission spectroscopy (ICP-OES) on an Optima 8300 instrument. Proton nuclear magnetic resonance (^1H NMR) data were collected using a Bruker Avance NEO 500 (500 MHz) system. The reaction intermediates were detected using in-situ Fourier-transform infrared spectroscopy (Thermo 6700). X-ray photoelectron spectroscopy (XPS) was performed by using a Thermo Scientific-ESCALAB Xi+ instrument. Synchrotron-based X-ray absorption fine structure (XAFS) spectra at the Cu and Ag K-edge were collected at BL14W1 station in Shanghai Synchrotron Radiation Facility (SSRF).

Electrochemical measurements

For electrode preparation, 1 mg of the catalyst was dispersed in 225 µL of isopropyl alcohol with 25 µL of Nafion via ultrasonication. The solution was then spread onto the carbon paper (1×1 cm^2) and dried overnight.

Electrocatalytic CO_2 reduction

Electrochemical experiments were carried out on a CHI 760E electrochemical workstation. All potentials were referenced to the reversible hydrogen electrode (RHE) unless otherwise specified. The conversion to RHE was done using E(vs. RHE) = E(vs. Ag/AgCl) + 0.197 V + 0.0591 × pH. Electrolysis experiments were performed in an H-type cell, equipped with a platinum gauze counter electrode and an Ag/AgCl reference electrode. Nafion-117 served as the proton exchange membrane, separating the cathode and anode compartments. The electrolyte was $KHCO_3$

aqueous solution (0.1 M), with 35 mL used per experiment. The catholyte was saturated with CO_2 by bubbling for 30 minutes before electrolysis.

Electrochemical surface area (ECSA) study

The cyclic voltammogram (CV) was performed in 0.1 M $KHCO_3$ solution using a three-electrode system. CV measurements were conducted from 0.1 to 0.5 V (vs. RHE) with various scan rates to obtain the double-layer capacitance (C_{dl}) of different catalysts. The C_{dl} was estimated by plotting the Δj ($j_a - j_c$) at 0.3 V (vs. RHE) against the scan rates, in which ja and jc were the anodic and cathodic current densities, respectively. The slope of this linear fit corresponds to twice the C_{dl}.

Product analysis

Gaseous products were quantified by a gas chromatograph (GC) equipped with a flame ionization detector (FID) for CO and CH_4 and a thermal conductivity detector (TCD) for H_2. Ultrapure Ar (99.999%) was used as the carrier gas. The liquid product was analyzed by ^{1}H NMR (Bruker Avance III 400 HD spectrometer) in deuterium oxide. The FE for each product was calculated using the following formula:

$$FE(\%) = \frac{ZNF}{Q}$$

Where *Z* is the number of electrons transferred, *N* is the number of moles for the product, *F* is the Faradaic constant of 96485 C mol−1, *Q* is the total charge passed during electrolysis.

In-situ attenuated total reflectance surface enhanced infrared absorption spectroscopy (ATR-SEIRAS) tests

The surface-enhanced infrared absorption spectroscopy (SEIRAS) with the attenuated total reflection (ATR) configuration was utilized to detect the reaction intermediates. A Thermo IS50 spectrometer equipped with an MCT detector cooled by liquid nitrogen was used for the ATR-SEIRAS measurements. To prepare the electrode, a Au thin film (around 60 nm) was deposited on Si prism. Before deposition, the Si prism surface was polished using diamond suspension and cleaned by sonication in water. The prism was then soaked in a piranha solution (7:3 volumetric ratio of 98% H_2SO_4 and 30% H_2O_2) for 2 hours to ensure surface cleanlines. 30 µL of ink was deposited and dried on the Au-film to serve as the working electrode. The ink-coated prism was then assembled into a homemade spectroelectrochemical cell. Hg/HgO was used as a reference, which was introduced near the working electrode via a Luggin capillary, and a Pt mesh (1 × 1 cm^2) was serving as the counter electrode. All spectra were expressed as $\Delta R/R = (E_s - E_R)/E_R$, where E_s and E_R represent the sample and reference spectra, respectively. The spectral resolution was set to 4 cm^{-1} for all the measurements. Throughout the experiment, CO_2 was continuously introduced into the electrolyte.

Calculation methods

All calculations were carried out using the Vienna Ab-initio Simulation Package (VASP) based on first-principles [1,2] within the framework of generalized gradient approximation (GGA) using the Perdew Burke Ernzerhof (PBE)[3] formulation. Projected augmented wave (PAW) potentials[4,5] were employed to describe the ionic cores. Valence electrons were represented by a plane wave basis set with a kinetic energy cutoff of 520 eV. Partial occupancies of the Kohn Sham orbitals were handled using the Gaussian smearing method with a smearing width of 0.05 eV. The electronic energy was considered self-consistent when the energy difference between iterations was less than 10^{-6} eV. A geometry optimization was considered convergent when the energy change was below 0.03 eV $Å^{-1}$. The vacuum spacing of 15 Å was maintained in a direction perpendicular to the surface of the structure. The Brillouin zone integration is performed using 3×3×1 Monkhorst Pack k-point sampling for the structure. The adsorption energies (E_{ads}) were calculated as $E_{ads} = E_{ad/sub} - E_{ad} - E_{sub}$, where $E_{ad/sub}$, E_{ad}, and E_{sub} are the total energies of the optimized adsorbate/substrate system, the adsorbate in the structure, and the clean substrate, respectively. The free energy was calculated using the equation:

$$G = E + ZPE - TS$$

Where G, E, ZPE, and TS are the free energy, total energy from DFT calculations, zero-point energy, and entropic contributions, respectively.

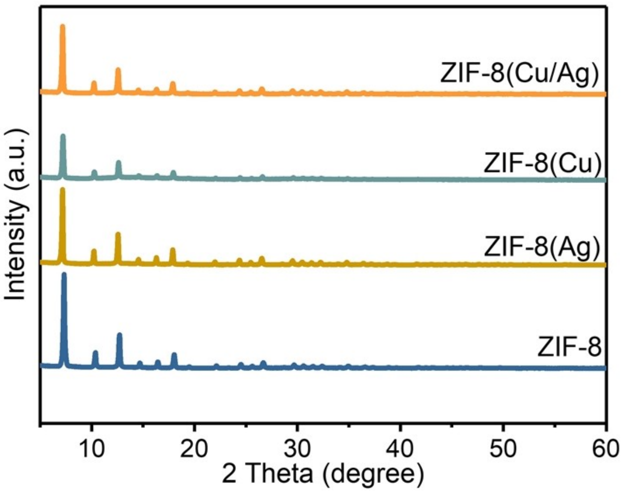

Fig. S1. XRD patterns of ZIF-8(Cu/Ag), ZIF-8(Cu), ZIF-8(Ag), and ZIF-8.

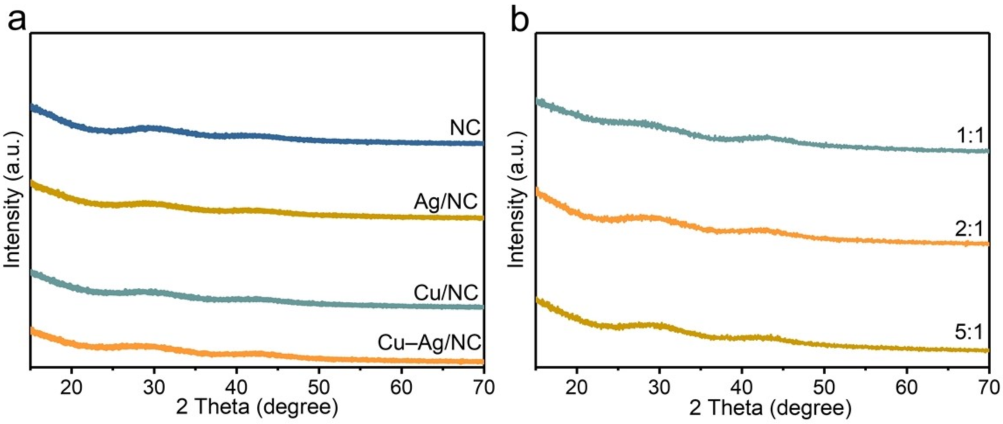

Fig. S2. a) XRD patterns of NC, Ag/NC, Cu/NC, and Cu–Ag/NC. b) XRD patterns of Cu–Ag/NC with different Cu/Ag ratios (1:1, 2:1, and 5:1).

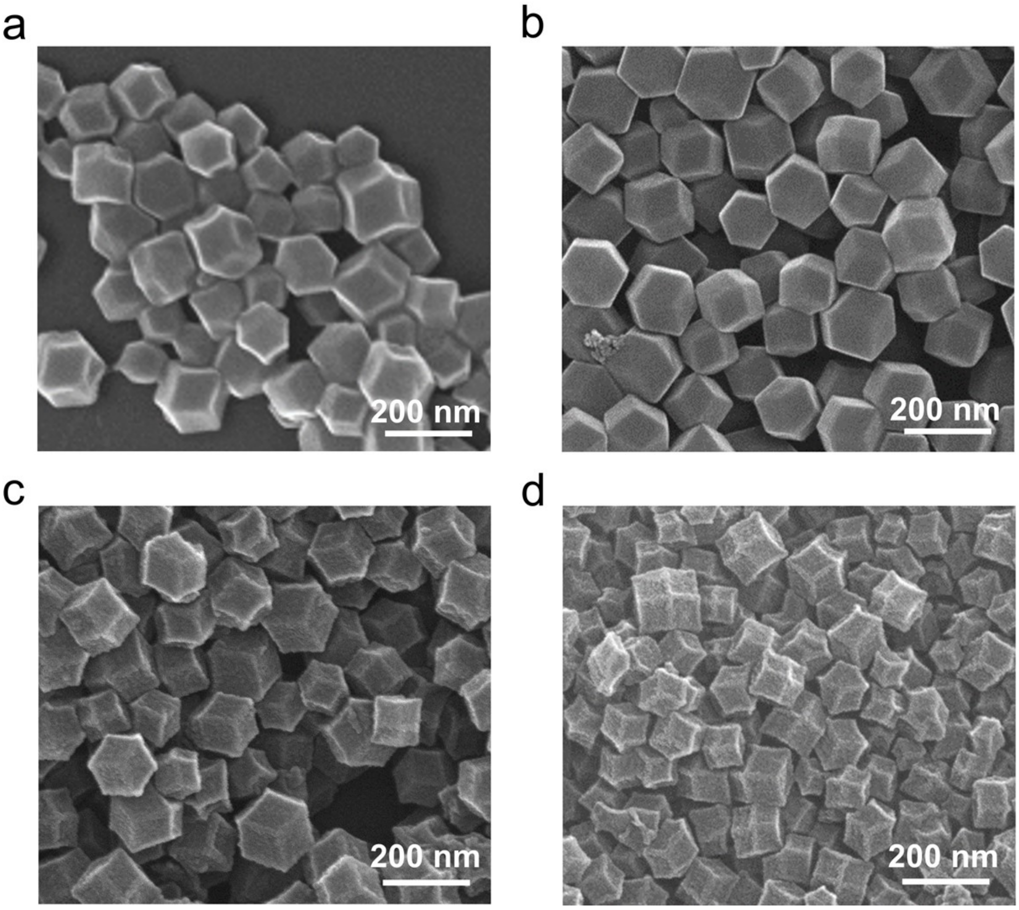

Fig. S3. SEM images of a) ZIF-8(Cu), b) ZIF-8(Ag), c) Cu/NC, and d) Ag/NC.

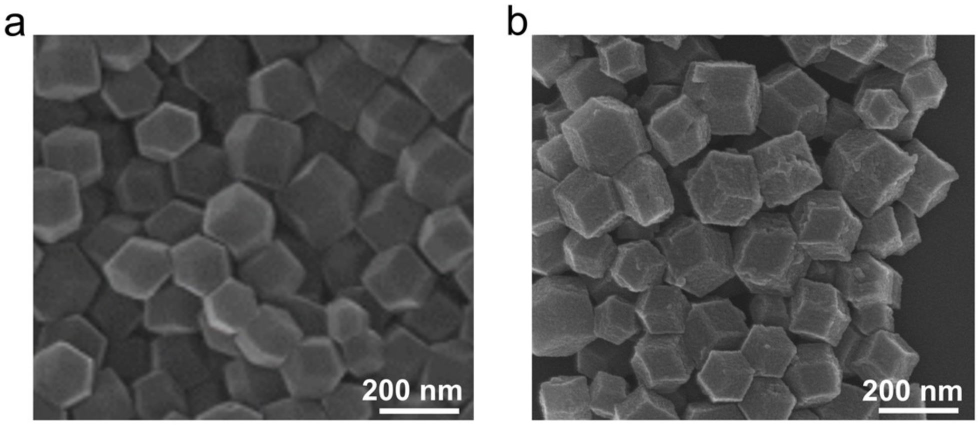

Fig. S4. SEM images of a) ZIF-8 and b) NC.

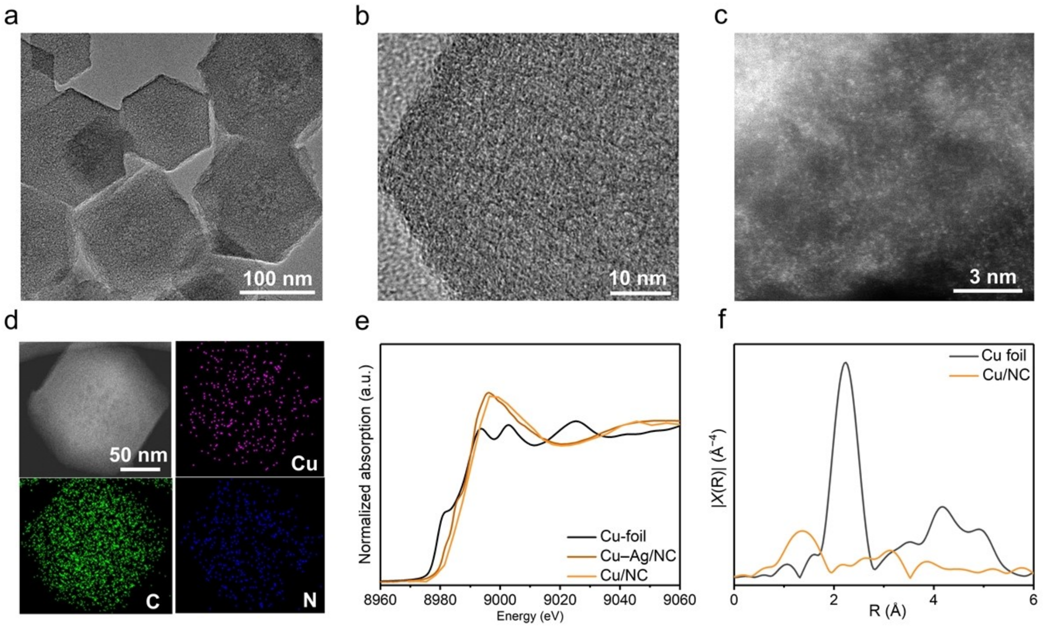

Fig. S5. a) TEM and b) high-resolution TEM images, c) aberration-corrected HAADF-STEM, and d) HAADF-STEM image and corresponding EDS elemental mapping images of Cu/NC. e) XAFS spectra of the Cu K-edge of Cu foil, Cu–Ag/NC, and Cu/NC. F) Fourier-transform EXAFS spectra of Cu foil, Cu–Ag/NC, and Cu/NC.

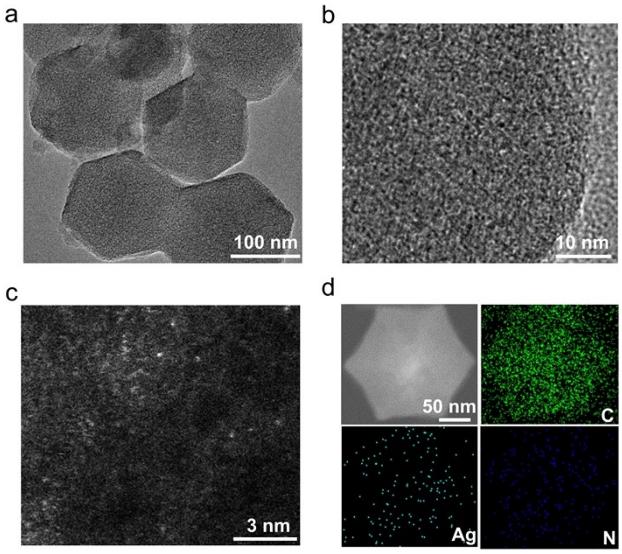

Fig. S6. a) TEM and b) high-resolution TEM images, c) aberration-corrected HAADF-STEM, and d) HAADF-STEM image and corresponding EDS elemental mapping images of Ag/NC.

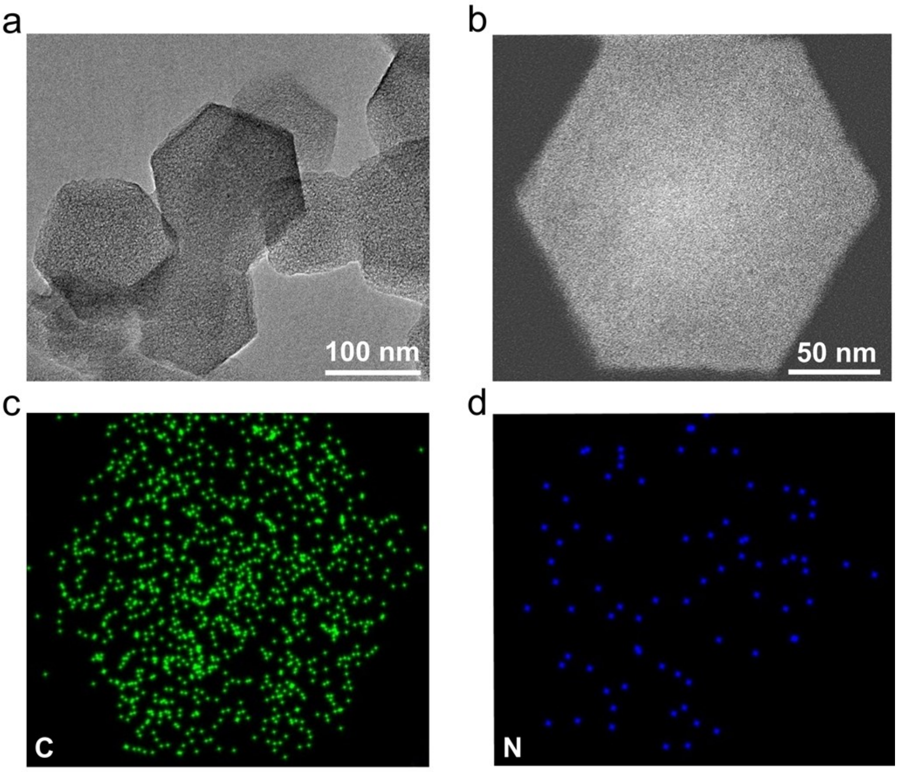

Fig. S7. a) TEM image, and b–d) HAADF-STEM image and corresponding EDS elemental mapping images of NC.

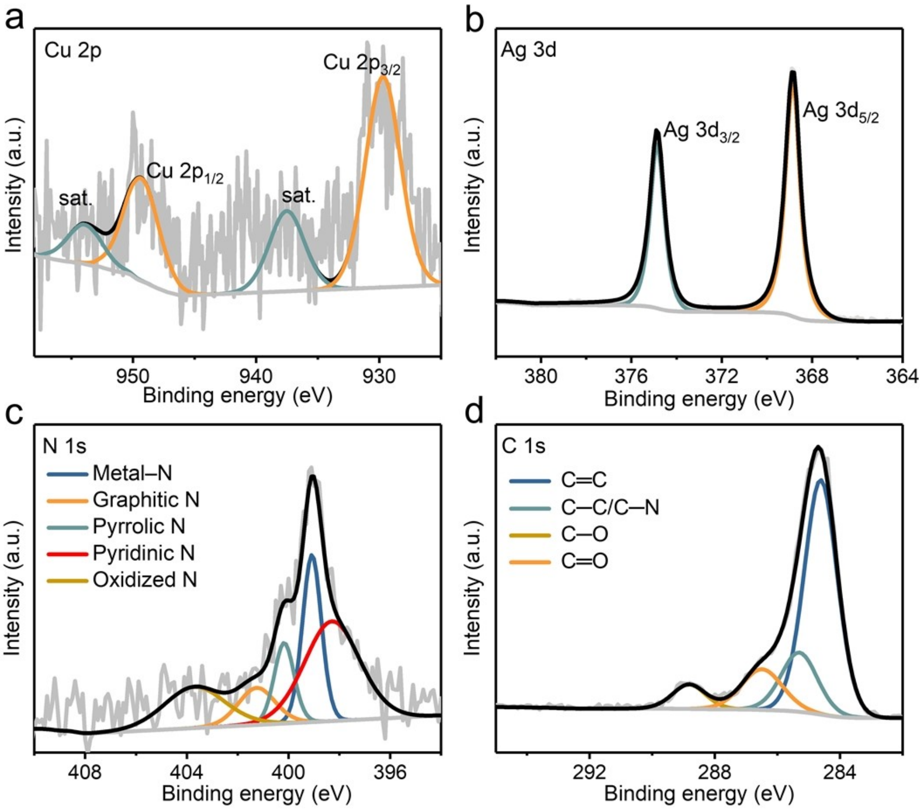

Fig. S8. a) Cu 2p, b) Ag 3d, c) N 1s, and d) C 1s XPS spectra of Cu–Ag/NC(1:1).

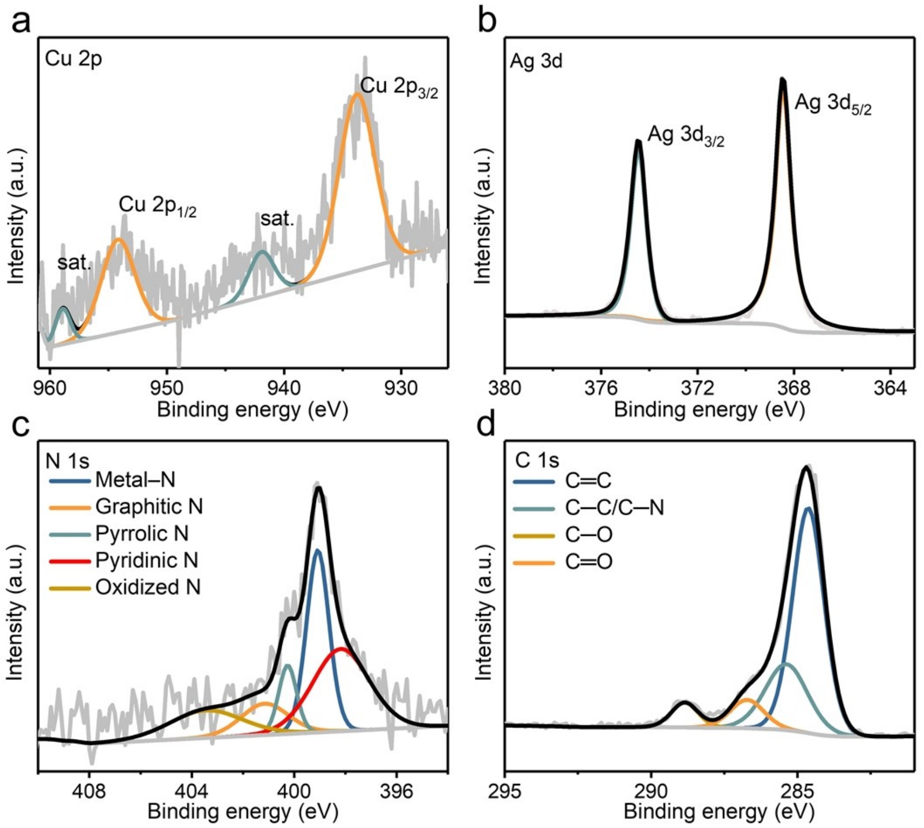

Fig. S9. a) Cu 2p, b) Ag 3d, c) N 1s, and d) C 1s XPS spectra of Cu–Ag/NC(5:1).

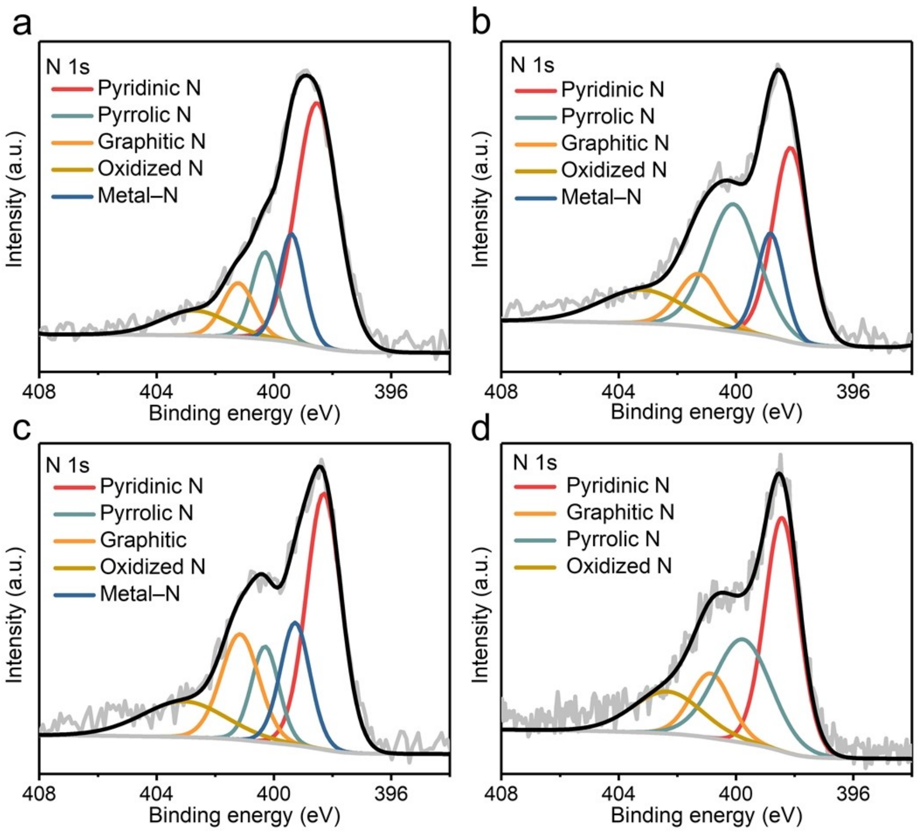

Fig. S10. N 1s XPS spectra of a) Cu–Ag/NC, b) Cu/NC, c) Ag/NC, and d) NC.

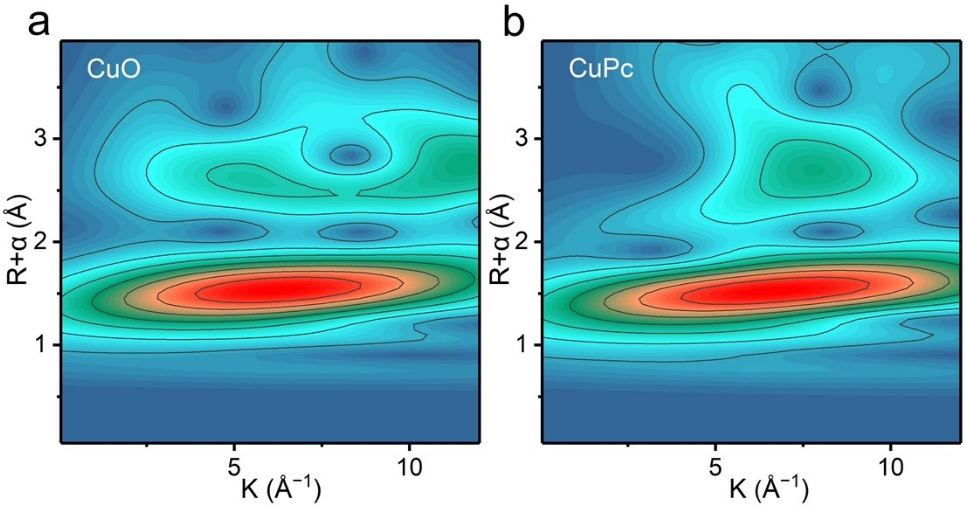

Fig. S11. WT plots of a) CuO and b) CuPc.

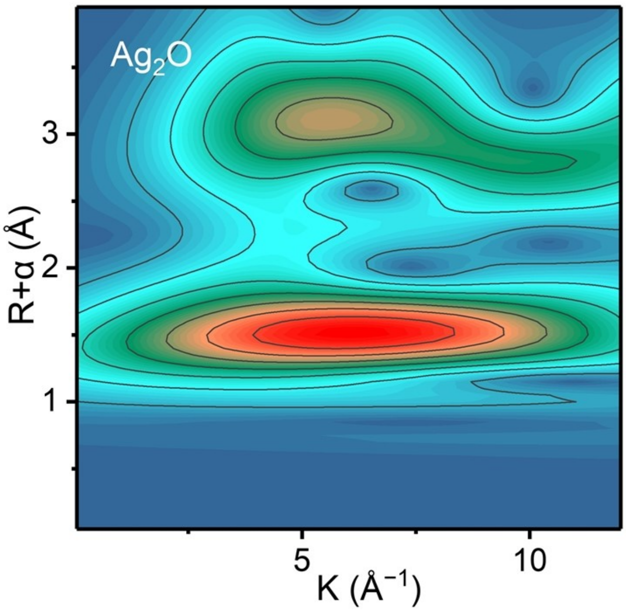

Fig. S12. WT plot of Ag$_2$O.

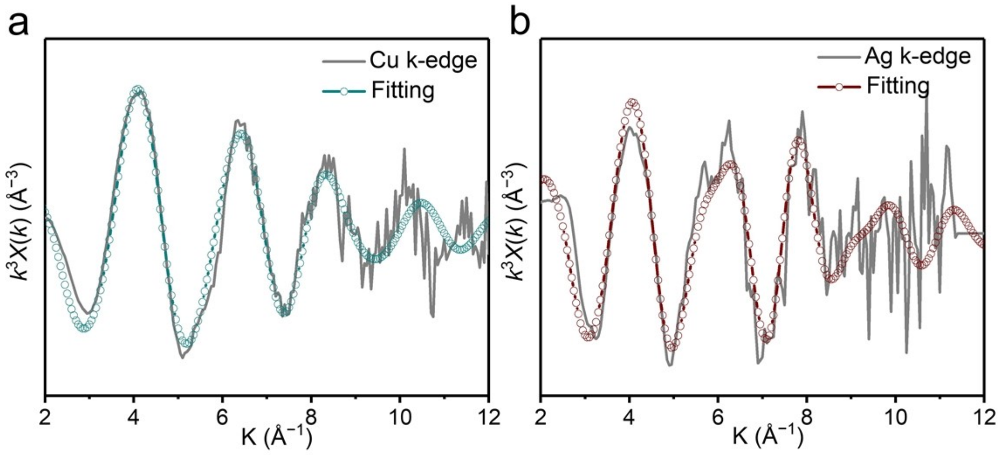

Fig. S13. Experimental and EXAFS fitting curves of a) Cu in Cu–Ag/NC and b) Ag in Cu–Ag/NC in k spaces.

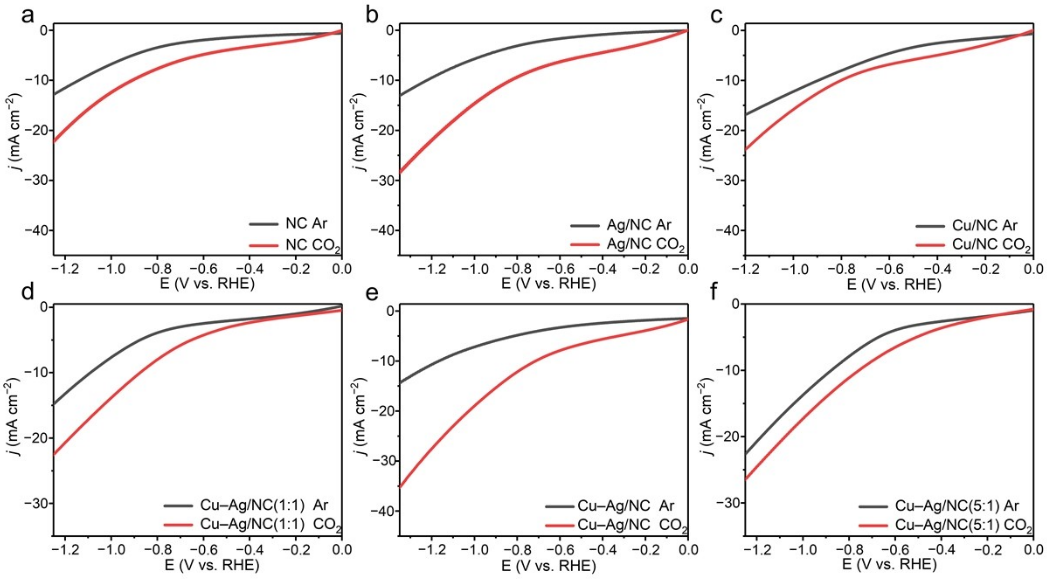

Fig. S14. LSV curves of a) NC, b) Ag/NC, c) Cu/NC, d) Cu–Ag/NC(1:1), e) Cu–Ag/NC, and f) Cu–Ag/NC(5:1) in CO_2 and Ar-saturated 0.1 M $KHCO_3$.

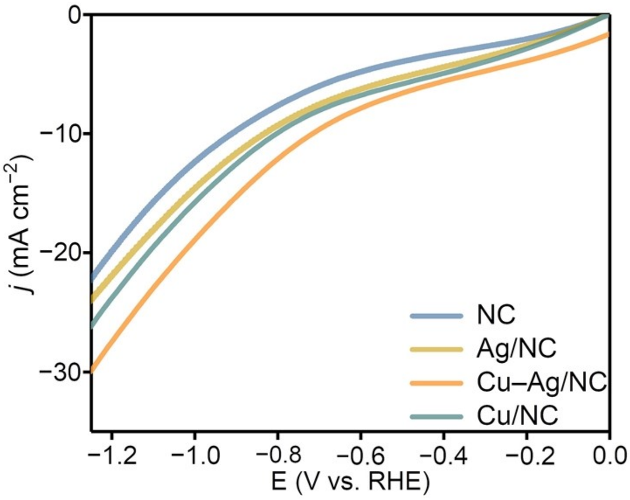

Fig. S15. LSV curves for catalysts obtained in CO_2-saturated 0.1 M $KHCO_3$ solution.

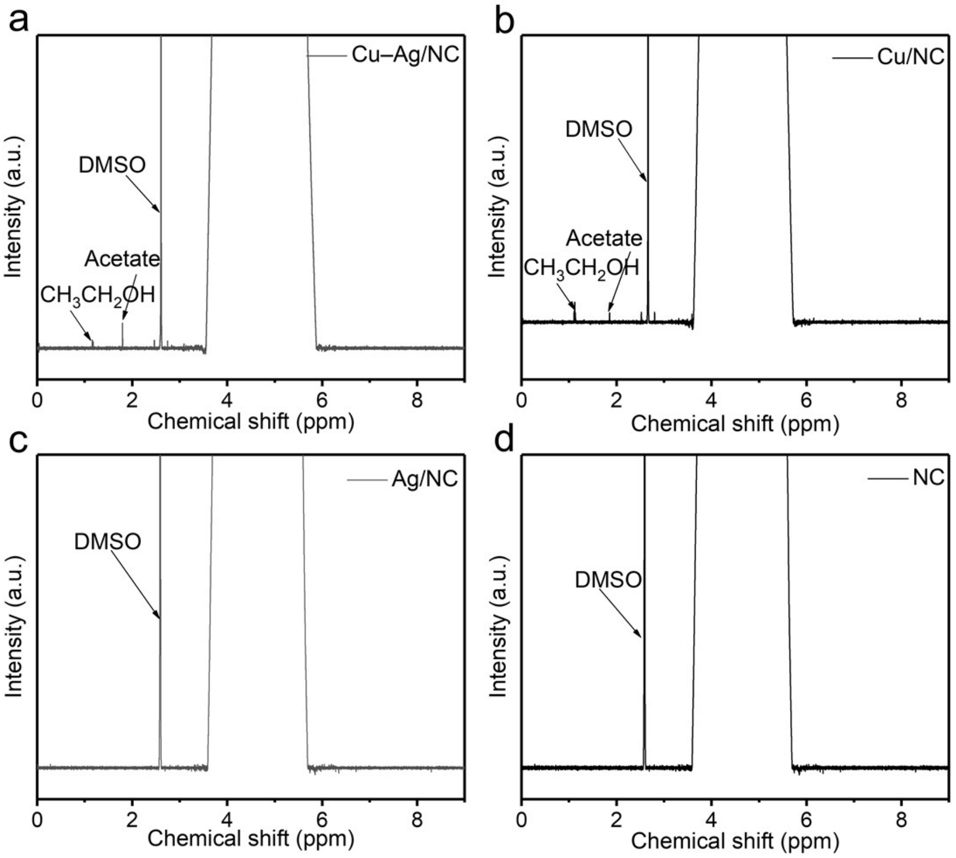

Fig. S16. ^{1}H nuclear magnetic resonance spectroscopy (^{1}H NMR) of the liquid products after potentiostatic electrolysis with a) Cu–Ag/NC, b) Cu/NC, c) Ag/NC, and d) NC.

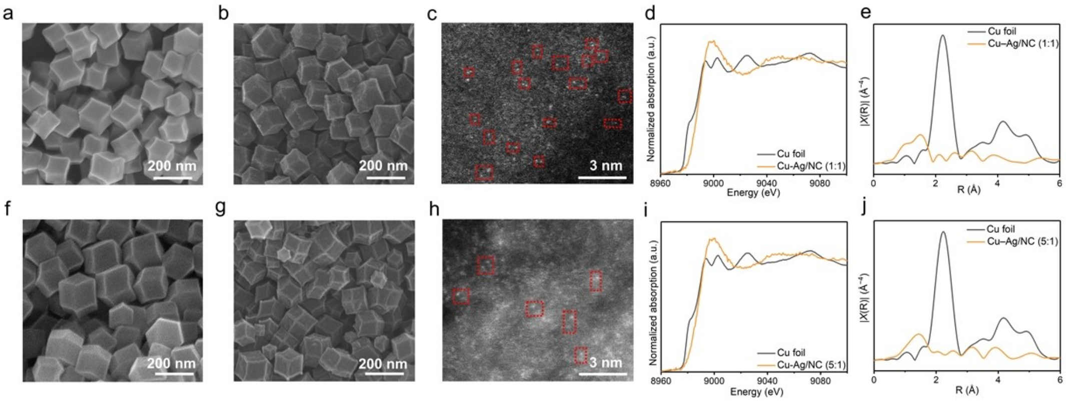

Fig. S17. SEM images of a) ZIF-8(Cu/Ag 1:1) and b) Cu–Ag/NC(1:1), c) aberration-corrected HAADF-STEM image of Cu–Ag/NC (1:1). d) XAFS spectra of the Cu K-edge of Cu foil and Cu–Ag/NC (1:1). e) Fourier-transform EXAFS spectra of Cu foil and Cu–Ag/NC (1:1). SEM images of f) ZIF-8(Cu/Ag 5:1) and g) Cu–Ag/NC(5:1), h) aberration-corrected HAADF-STEM image of Cu–Ag/NC (5:1). i) XAFS spectra of the Cu K-edge of Cu foil and Cu–Ag/NC (5:1). j) Fourier-transform EXAFS spectra of Cu foil and Cu–Ag/NC (5:1).

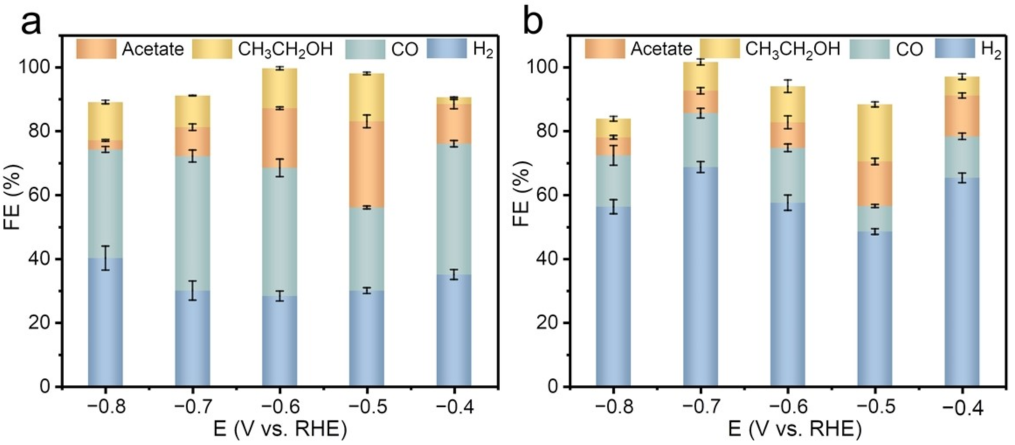

Fig. S18. FE of all the products obtained on a) Cu–Ag/NC(1:1) and b) Cu–Ag/NC(5:1).

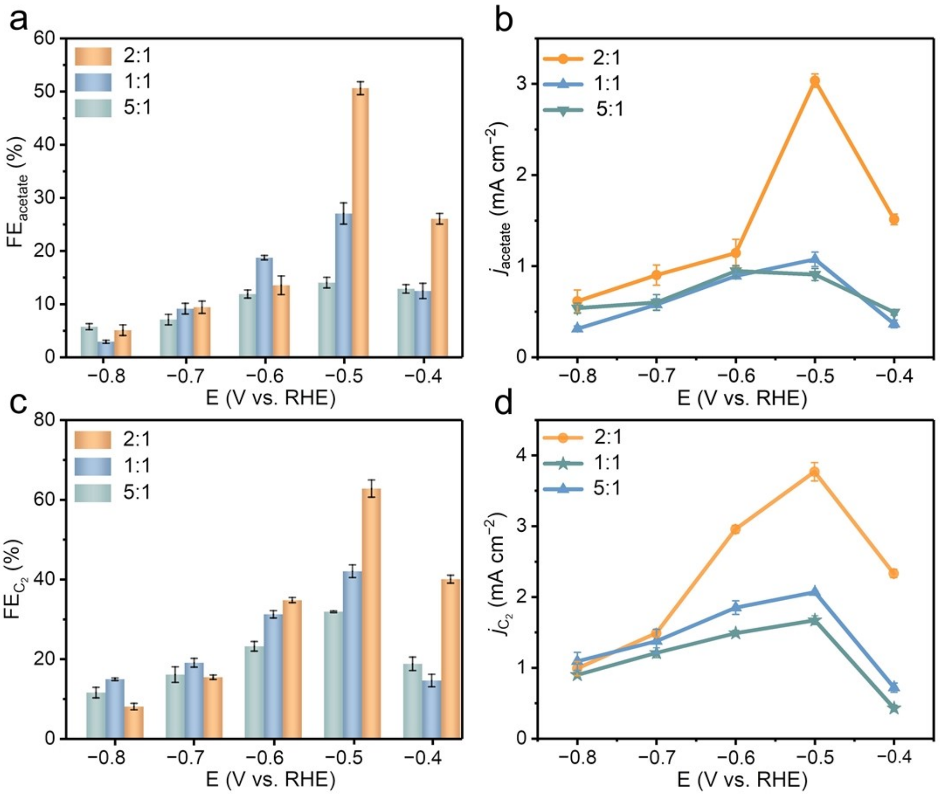

Fig. S19. a) FE$_{acetate}$, b) $j_{acetate}$, c) FE$_{C2}$, and d) j_{C2} for CO_2RR over Cu–Ag/NC with different Cu and Ag ratios (1:1, 2:1, and 5:1).

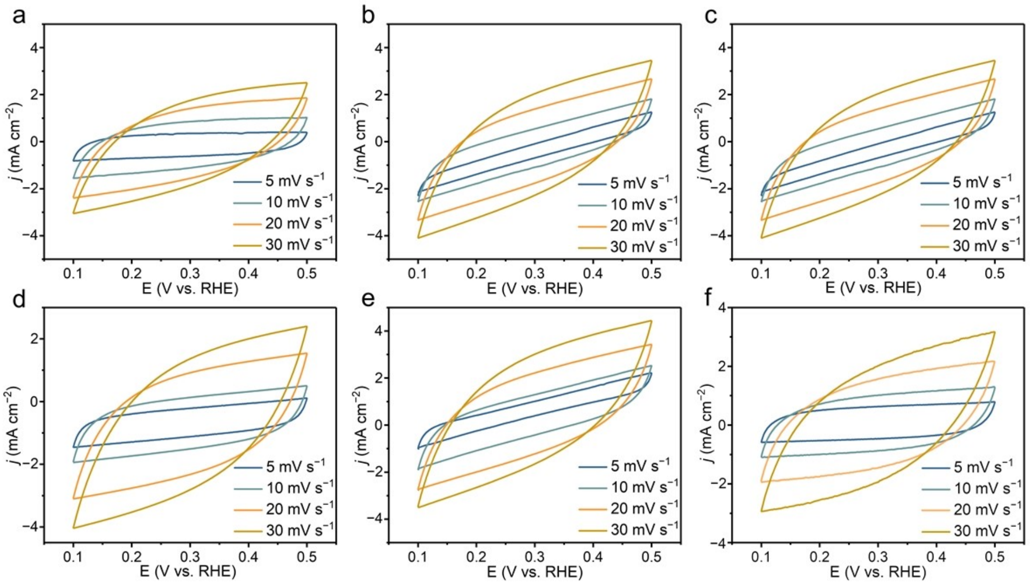

Fig. S20. CVs of a) NC, b) Cu/NC, c) Ag/NC, d) Cu–Ag/NC(1:1), e) Cu–Ag/NC, and f) Cu–Ag/NC(5:1) in 0.1 M $KHCO_3$ electrolyte at different scan rates.

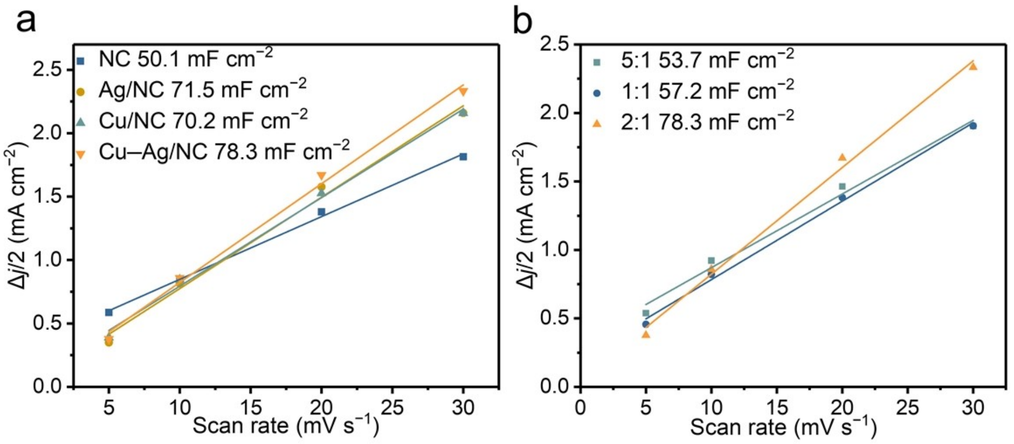

Fig. S21. The measured C_{dl} for a) NC, Ag/NC, Cu/NC, and Cu–Ag/NC and b) Cu–Ag/NC with different Cu and Ag ratios (1:1, 2:1, and 5:1).

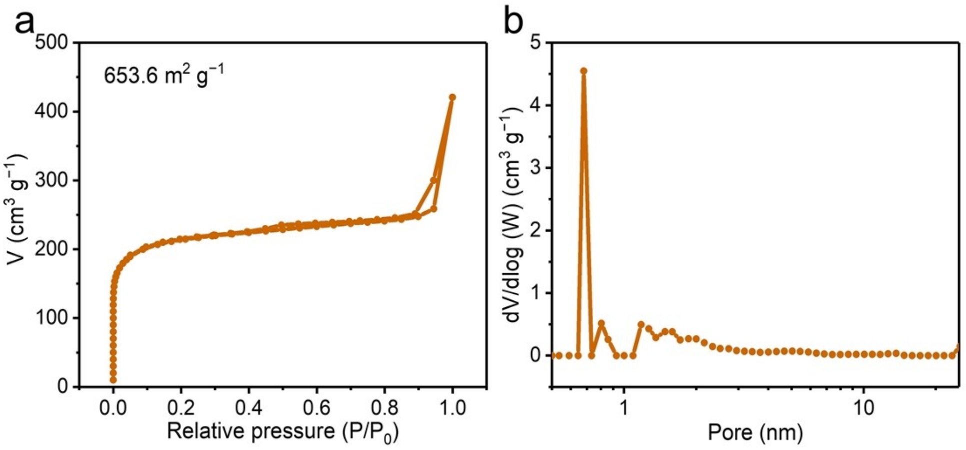

Fig. S22. a) Nitrogen adsorption/desorption isotherms and b) pore size distribution of Cu–Ag/NC.

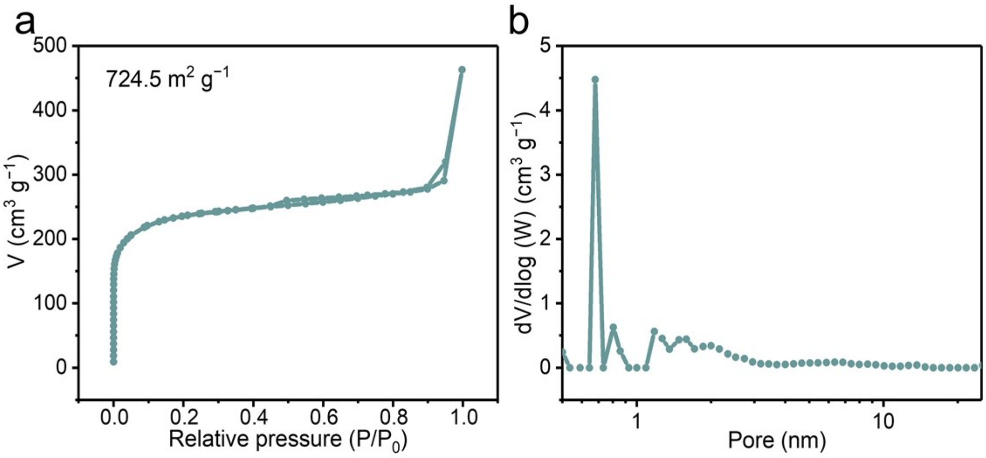

Fig. S23. a) Nitrogen adsorption/desorption isotherms and b) pore size distribution of Cu/NC.

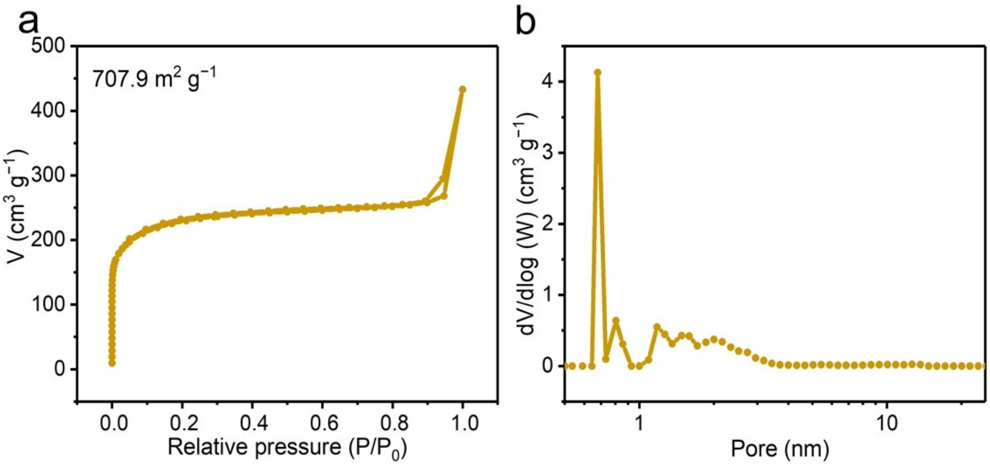

Fig. S24. a) Nitrogen adsorption/desorption isotherms and b) pore size distribution of Ag/NC.

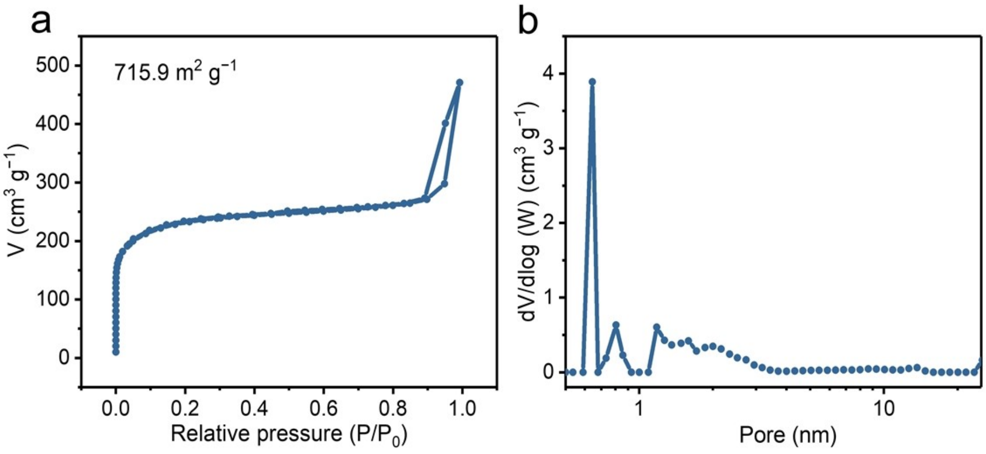

Fig. S25. a) Nitrogen adsorption/desorption isotherms and b) pore size distribution of NC.

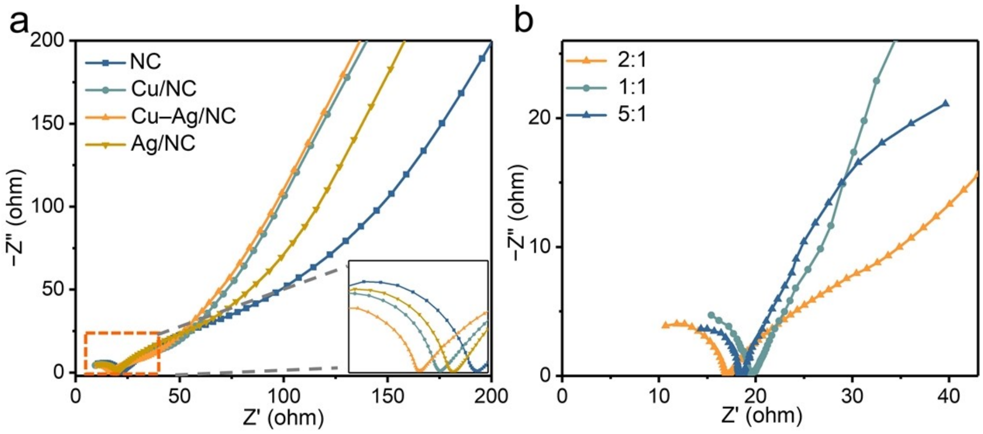

Fig. S26. Nyquist plots of a) NC, Cu/NC, Ag/NC, and Cu–Ag/NC and b) Cu–Ag/NC with different Cu and Ag ratios (1:1, 2:1, and 5:1) in CO_2-saturated 0.1 M $KHCO_3$ electrolyte.

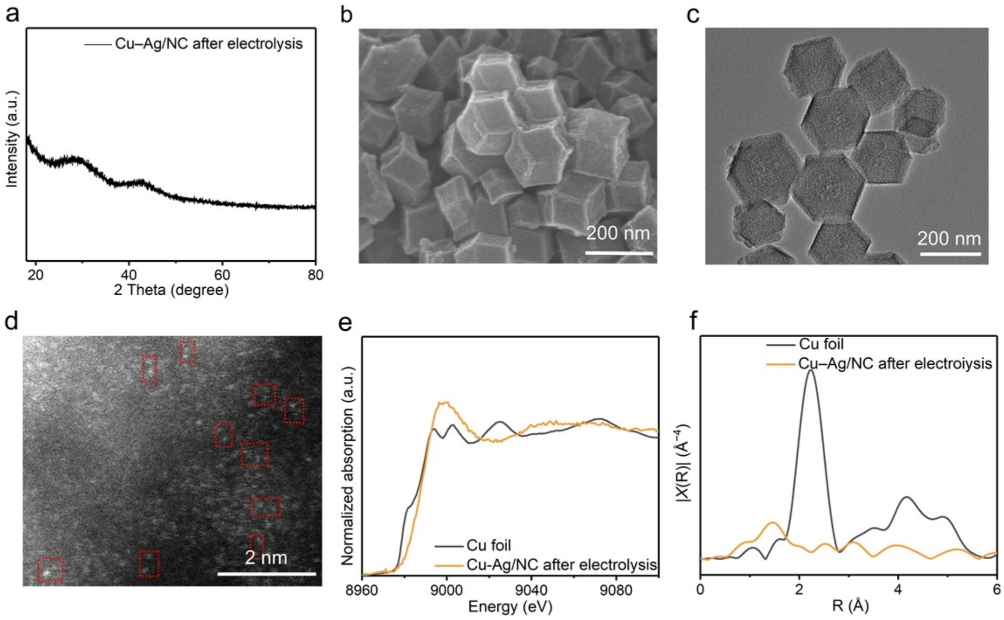

Fig. S27. a) XRD patterns, b) SEM, c) TEM, d) aberration-corrected HAADF-STEM images of Cu–Ag/NC. e) XAFS spectra of the Cu K-edge of Cu foil and Cu–Ag/NC. f) Fourier-transform EXAFS spectra of Cu foil and Cu–Ag/NC after the electrolytic CO_2RR.

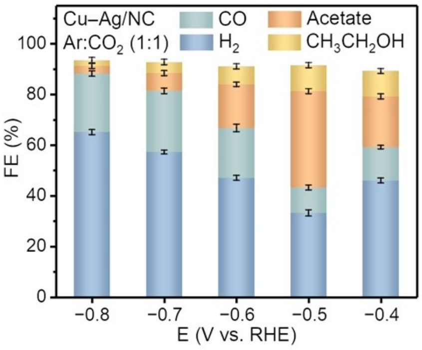

Fig. S28. The product FEs of Cu–Ag/NC at different potentials in CO_2:Ar (1:1)-saturated 0.1 M $KHCO_3$ electrolyte.

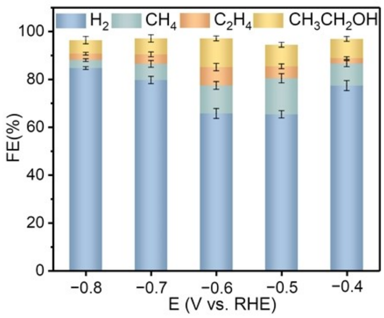

Fig. S29. The product FEs of Cu–Ag/NC at different potentials in CO-saturated 0.1 M $KHCO_3$ electrolyte.

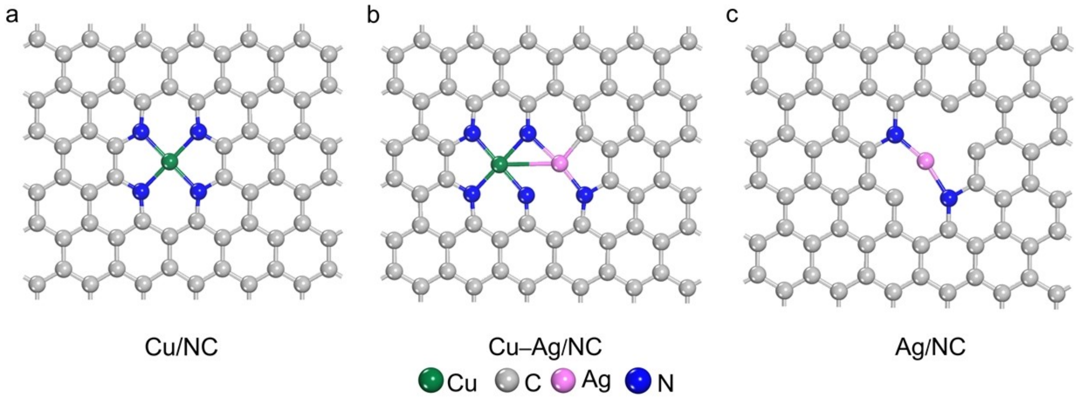

Fig. S30. Top views of a) Cu/NC, b) Cu–Ag/NC, and c) Ag/NC.

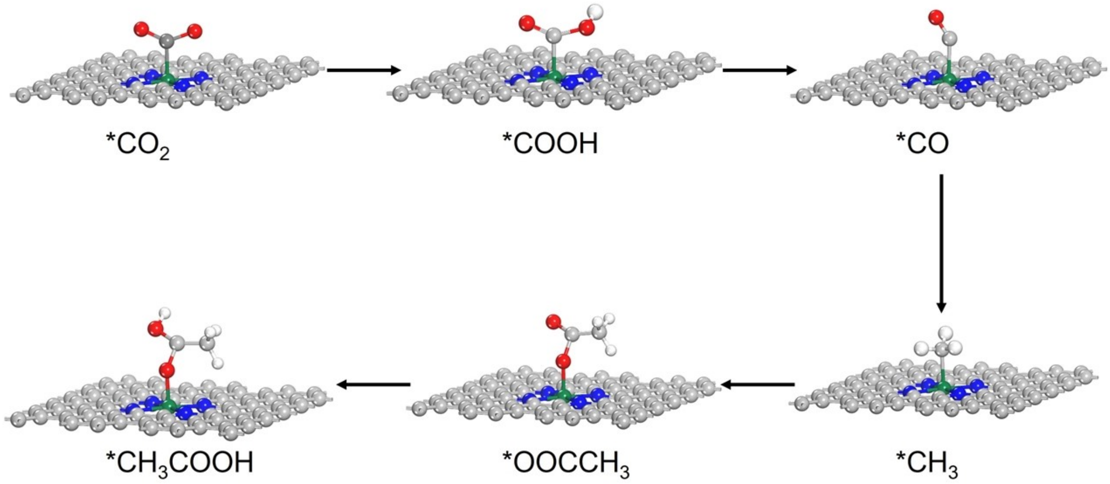

Fig. S31. Proposed reaction pathways for the conversion of CO_2 to CH_3COOH on Cu/NC.

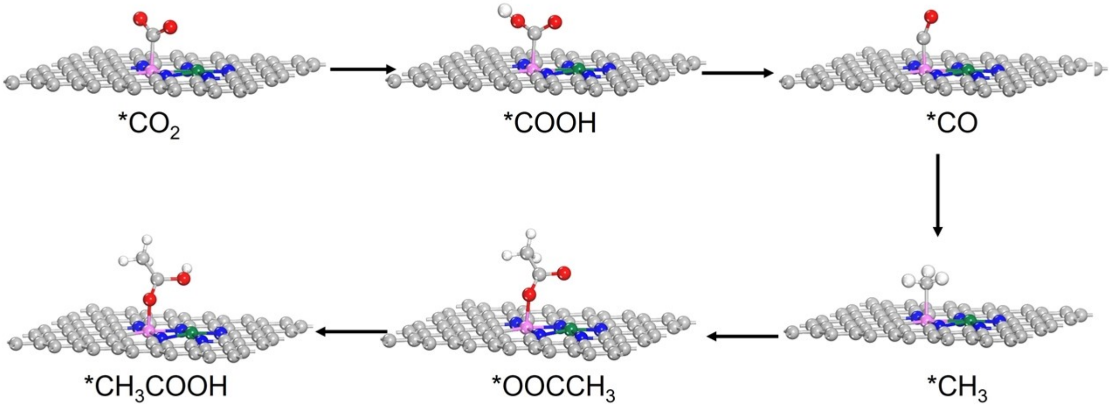

Fig. S32. Proposed reaction pathways for the conversion of CO_2 to CH_3COOH on Ag in Cu–Ag/NC.

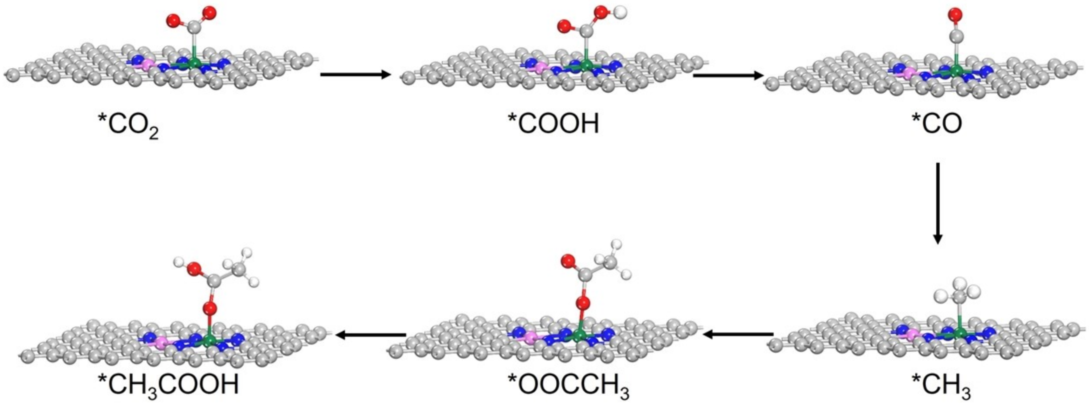

Fig. S33. Proposed reaction pathways for the conversion of CO_2 to CH_3COOH on Cu in Cu–Ag/NC.

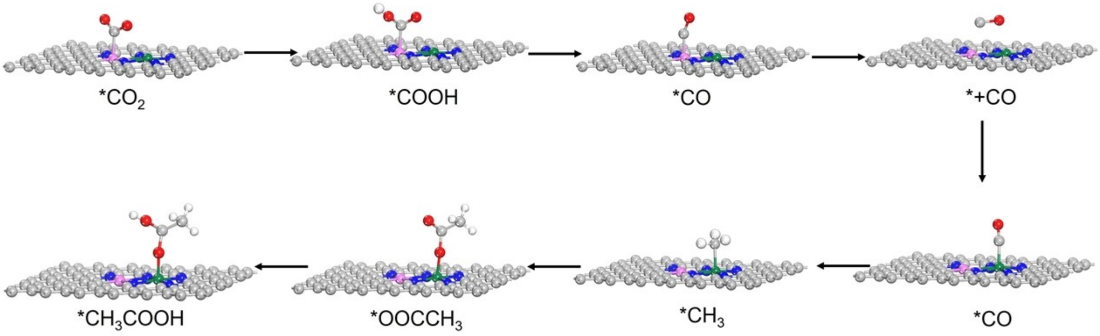

Fig. S34. Proposed reaction pathways for the conversion of CO_2 to CH_3COOH on Cu–Ag/NC.

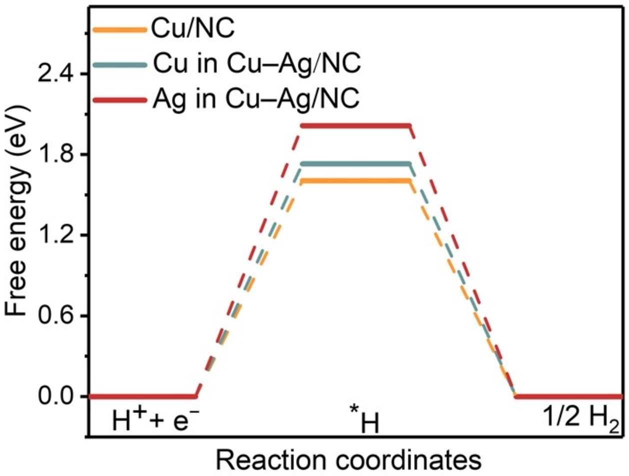

Fig. S35. Calculated free energy of HER over different catalyst models.

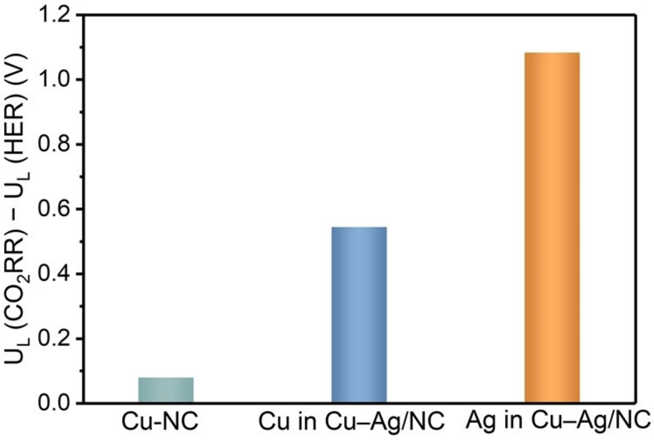

Fig. S36. Limiting potential differences for CO_2RR and HER on different active models at U = 0 V vs. RHE.

Table S1. The metal loadings of Cu–Ag/NC(1:1), Cu–Ag/NC, Cu–Ag/NC(5:1), Cu/NC, and Ag/NC determined by ICP-OES.

Samples	Cu contents (wt%)	Ag contents (wt%)
Cu–Ag/NC	0.69	0.42
Cu/NC	0.68	/
Ag/NC	/	0.46
Cu–Ag/NC(1:1)	0.36	0.25
Cu–Ag/NC(5:1)	1.46	0.35

Table S2. EXAFS fitting parameters of the Cu foil, Ag foil, and Cu–Ag/NC samples.

Samples	Shell	CN	R(Å)	σ^2	ΔE_0	R factor
Cu foil	Cu–Cu	12	2.54±0.01	0.0086	4.5±0.4	0.0025
Ag foil	Ag–Ag	12	2.86±0.01	0.0095	1.1±0.3	0.0029
Cu–Ag/NC	Cu–N	3.8±0.3	1.94±0.01	0.0086	−7.8±2.1	0.0198
	Cu–Ag	0.6±0.3	2.60±0.05	0.0146	/	/
	Ag–N	1.8±0.1	2.14±0.02	0.0085	−3.0±2.0	0.0118
	Cu–Ag	1.1±0.2	2.80±0.02	0.0153	/	/

CN: coordination numbers; R: bond distance; σ^2: Debye-Waller factors; ΔE_0: the inner potential correction. R factor: goodness of fit. S_0^2 was set to 0.86, according to the experimental EXAFS fit of Ag foil and Cu foil reference by fixing CN as the known crystallographic value.

Table S3. Summary of the performances of electrocatalysts for CO_2RR to acetate.

Catalysts	Potential (V vs. RHE)	Electrolyte	$FE_{acetate}$ (%)	$j_{acetate}$ (mA cm^{-2})	Stability (h)	Ref.
Cu–Ag/NC	−0.5	0.1 M $KHCO_3$	50	3	30	This work
Cu-Cu_2O/Cu	−0.4	0.1 M KCl	40	3.2	7	[6]
Mo_8@Cu/TNA	−0.8	$NaHCO_3$	28.8	17.3	3	[7]
Fe/NC	−0.5	0.05 M $KHCO_3$	61	0.061	/	[8]
Cu_{10}-CNT	−0.8	0.5 M $KHCO_3$	56	9.3	/	[9]
Cu_2(CuTCPP)	−1.55	CH_3CN solution with 1 M H_2O and 0.5 M $EMIMB_4$	16.8	0.5	1	[10]
Cu_2Ag_3/polymer/GCE	−1.33	0.5 M $KHCO_3$	21.2	/	/	[11]
Cu/Cu_xOF	−0.3	1 M KOH	27	4	/	[12]
Mn-TPPS	−0.8	0.1 M $KHCO_3$	62	/	6	[13]
PcNi-DMTP/MAF-2	/	1 M KOH	51.2	410	200	[14]
G_3-NH_2/Cu	−0.97	1 M KOH	47	202	> 100	[15]

References

1 G. Kresse and J. Furthmuller, *Comp. Mater. Sci.*, 1996, **6**, 15–50.
2 G. Kresse and J. Furthmuller, *Phys. Rev. B.*, 1996, **54**, 11169–11186.
3 J. P. Perdew, K. Burke, and M. Ernzerhof, *Phys. Rev. Lett.*, 1996, **77**, 3865–3868.
4 G. Kresse, and D. Joubert, *Phys. Rev. B.*, 1999, **59**, 1758–1775.
5 P. E. Blochl, *Phys. Rev. B.*, 1994, **50**, 17953–17979.
6 Q. Zhu, X. Sun, D. Yang, J. Ma, X. Kang, L. Zheng, J. Zhang. Z. Wu, and B. Han, *Nat. Commun.*, 2019, **10**, 3851.
7 D. Zang, Q. Li, G. Dai, M. Zeng, Y. Huang, and Y. Wei, *Appl. Catal. B: Environ.*, 2021, **281**, 119426.
8 C. Genovese, M. E. Schuster, E. K Gibson, D. Gianolio, V. Posligua, R. Grau-Crespo, G. Cibin, P. P. Wells, D. Garai, V, Solokha, S. K. Calderon, J. J. Velasco-Velez, C. Ampelli, S. Perathoner, G. Heid, G. Cent, and R. Arrigo, *Nat. Commun.*, 2018, **9**, 935.
9 C. Genovese, C. Ampelli, S. Perathoner, and G. Centi, *Green Chem.*, 2017, **19**, 2406–2415.
10 J.-X. Wu, S.-Z. Hou, X.-D. Zhang, M. Xu, H.-F. Yang, P.-S. Cao, and Z.-Y. Gu, *Chem. Sci.*, 2019, **10**, 2199–2205.
11 Y. Wang, D. Wang, C. J. Dares, S. L. Marquard, M. V. Sheridan, and T. J. Meyer, *Proc. Natl. Acad. Sci. U.S.A.*, 2018, **115**, 278–283.
12 R. Cai, M. Sun, J. Ren, M. Ju, X. Long, B. Huang, and S. Yang, *Chem. Sci.*, 2021, **12**, 15382.
13 M. Abdinejad, T. Yuan, K. Tang, S. Duangdangchote, A. Farzi, H.-P. I. V. Montfort, M. Li, J. Middelkoop, M. Wolff, A. Seifitokaldani, O. Voznyy, and T. Burdyny, *Chem. Eur. J.*, 2023, **29**, e202203977.
14 H.-L. Zhu, J.-R. Huang, M.-D. Zhang, C. Yu, P.-Q. Liao, and X.-M. Chen, *J. Am. Chem. Soc.*, 2024, **146**, 1144–1152.
15 L. Yang, X. Lv, C. Peng, S. Kong, F. Huang, Y. Tang, L. Zhang, and G. Zheng, *ACS Cent. Sci.*, 2023, **9**, 1905–1912.